

# Data assimilation and resolvent analysis of turbulent flow behind a wall-proximity rib

Cite as: Phys. Fluids **31**, 025118 (2019); <https://doi.org/10.1063/1.5074151>

Submitted: 22 October 2018 . Accepted: 02 February 2019 . Published Online: 22 February 2019

Chuangxin He , Yingzheng Liu , Lian Gan , and Lutz Lesshafft



View Online



Export Citation



CrossMark

## ARTICLES YOU MAY BE INTERESTED IN

[Missing data recovery using data fusion of incomplete complementary data sets: A particle image velocimetry application](#)

Physics of Fluids **31**, 025105 (2019); <https://doi.org/10.1063/1.5079896>

[Three dimensional structure of the unsteady wake of an axisymmetric body](#)

Physics of Fluids **31**, 025113 (2019); <https://doi.org/10.1063/1.5078379>

[Referee acknowledgment for 2018](#)

Physics of Fluids **31**, 020201 (2019); <https://doi.org/10.1063/1.5090536>



# Data assimilation and resolvent analysis of turbulent flow behind a wall-proximity rib

Cite as: *Phys. Fluids* **31**, 025118 (2019); doi: [10.1063/1.5074151](https://doi.org/10.1063/1.5074151)

Submitted: 22 October 2018 • Accepted: 2 February 2019 •

Published Online: 22 February 2019



Chuangxin He,<sup>1,2,3</sup> Yingzheng Liu,<sup>1,2,4,a)</sup> Lian Gan,<sup>3</sup> and Lutz Lesshafft<sup>5</sup>

## AFFILIATIONS

<sup>1</sup>Key Lab of Education Ministry for Power Machinery and Engineering, School of Mechanical Engineering, Shanghai Jiao Tong University, 800 Dongchuan Road, Shanghai 200240, China

<sup>2</sup>Gas Turbine Research Institute, Shanghai Jiao Tong University, 800 Dongchuan Road, Shanghai 200240, China

<sup>3</sup>Department of Engineering, Durham University, Stockton Road, Durham DH1 3LE, United Kingdom

<sup>4</sup>Collaborative Innovation Center for Advanced Ship and Deep-Sea Exploration, Shanghai Jiao Tong University, Shanghai 200240, China

<sup>5</sup>Laboratoire d'Hydrodynamique, CNRS – École Polytechnique, Palaiseau 91128, France

<sup>a)</sup> Author to whom correspondence should be addressed: [yzliu@sjtu.edu.cn](mailto:yzliu@sjtu.edu.cn)

## ABSTRACT

This study aims to detect the unsteady features of the turbulent flow behind a wall-proximity rib using resolvent analysis, based on the mean flow field determined using an adjoint-based data assimilation (ABDA) model. The rib is located at gap ratios  $G/d = 0.25$  and  $0.50$  with a flow Reynolds number  $Re = 7600$  based on the rib size ( $d = 10$  mm) and the free-stream velocity  $U_0$ . The split fiber measurements at  $x/d = -0.25, 1.25, 4.25,$  and  $9.25$  are solely used as observational data, while the temperature sensitive paint and particle image velocimetry (PIV) results are used as the complement for the analysis and validation. First, the mean flows at both gap ratios are reproduced with the ABDA model using the streamwise velocity constraint of the observational data. It is shown that the global fields are accurately recovered, including the wall jet originating from the gap, which is absent from the PIV results. This finding indicates substantial heat transfer enhancement immediately behind the rib. Subsequently, the resolvent modes at Strouhal numbers  $St = 0.02, 0.05, 0.15,$  and  $0.30$  are obtained from the mean flows using a stochastic approach instead of performing the singular value decomposition directly on the resolvent operator, due to the large matrix size. With the help of the power spectral density of the split fiber measurement, the resolvent analysis identifies the large-scale flapping motion and the wall-jet fine scales that enhance the heat transfer in the case of  $G/d = 0.25$ , in addition to the Karman vortex shedding, which makes little contribution to the wall heat transfer in the case of  $G/d = 0.50$ . The flow dynamical features in both cases are reconstructed using the leading five resolvent modes at  $St = 0.15$ , showing good agreement with the proper orthogonal decomposition modes.

Published under license by AIP Publishing. <https://doi.org/10.1063/1.5074151>

## I. INTRODUCTION

Unsteadiness of wall-bounded turbulent shear and separated flows, which is inherently linked with superimposed energetic flow structures, is highly desirable for wall heat removal in various industrial applications such as gas turbines and electronics manufacture.<sup>1,2</sup> However, accurate determination of such high degree-of-freedom systems poses a challenge for costly scale-resolved simulations such as detached

eddy simulation (DES) and large eddy simulation (LES), while highly spatio-temporally varying flow behaviors near the wall incur substantial difficulties in velocity field measurements even when using state-of-the-art time-resolved particle image velocimetry (PIV). Alternatively, a substantial quantity of research has been devoted to constructing a reduced-order description of the flow behaviors<sup>3-6</sup> by complementing computational fluid dynamics and experimental measurements. Among these strategies, resolvent analysis

serves as an effective approach to determine the optimal response of a flow system to turbulence excitation and then trigger the energetic unsteady flow structures; such analysis can be derived from the mean flow field, along with the Fourier spectra of flow quantities at selected positions for mode amplitude calibration.

Many approaches have been developed to identify the unsteadiness features of flows. For this purpose, a proper orthogonal decomposition (POD)-based reduced-order model (ROM) is usually used, by simplifying the entire flow dynamics to a system of ordinary differential equations, which has much lower dimensions than the original turbulence system.<sup>7,8</sup> However, this approach suffers from computational instability when conducting time-integration. Although a data assimilation strategy has been implemented to reduce the computational instability,<sup>4</sup> POD spatial modes must be determined in advance, which requires high-resolution, accurate measurements in the global field of interest. This disadvantage also holds for linear stochastic estimation (LSE),<sup>9,10</sup> in which time evolution of large-scale structures is estimated by coupling spatial POD modes and time-resolved point measurements. Alternative approaches<sup>11,12</sup> involving data-driven procedures to predict the unsteady flow fields have high demand of experimental data and computational efforts.

Given an accurate mean flow field, large-scale modes can barely be acquired by analyzing the governing equations. In this regard, a non-rigorous realization is to apply linear stability analysis (LSA) on the mean flow, capturing the evolution of small perturbations upon the steady mean flow that is forced by the Reynolds stress. It should be noted that nonlinear effects may thus be factored compared with the base-flow stability analysis.<sup>13,14</sup> Barkly<sup>15</sup> showed that LSA predicted a cylinder wake's frequency fairly well, with a marginally stable global mode representing Karman vortex shedding. However, the difference in the spatial patterns between this global mode and the Fourier mode of the cylinder wake has never been explained. The most reasonable explanation is that LSA still lies in the linear regime and predicts stability modes without self-interaction. It has also been shown that LSA performed on the mean flow is not always relevant while the condition of mean flow harmonic dominates; the second harmonic must be fulfilled to capture the correct frequency and the corresponding marginally stable mode.<sup>16</sup> Although nonlinear stability analysis tools have been developed,<sup>17-19</sup> the time-dependent solution procedures are time-consuming and the multi-scale approach has limited applicability in turbulent flows.

A more rigorous approach compared to the LSA, named resolvent analysis, has been proposed. This type of analysis involves exploring the optimal flow response to the global forcing, which is regarded as non-linear Reynolds stress when analysis is performed on the mean flow.<sup>20</sup> The optimal response (resolvent modes) can be obtained by singular value decomposition (SVD) of the resolvent operator and thus can be used to reconstruct the unsteady flow field through linear combination. Beneddine *et al.*<sup>21,22</sup> noted that when the flow is convective-unstable and the singular value is

significantly larger than all others, the unsteady flow field can be reconstructed using only the first resolvent mode and the mean field; successful application was demonstrated by reconstructing an unsteady jet from the mean field and pointwise measurements. It is notable that flow dynamic deduction based on resolvent analysis is generally valid for various flow configurations. The only difference for convective-unstable flow and other types is the number of resolvent modes and pointwise measurements required for reconstruction. Nonetheless, determination of the mean flow is tricky, as once it is obtained using sophisticated simulations or experimental measurements, the flow dynamics are usually obtained in detail; however, it is hard to experimentally measure the complete global field of the mean flow, which is required for calculating the resolvent operator. In this sense, the novel adjoint-based data assimilation (ABDA) model proposed by the authors<sup>23</sup> shows great advantages in determining the mean flow from very limited pointwise measurement data; it does so by introducing a spatially varying correction function (determined by a continuous adjoint process) into the turbulence model to remedy the global balance of turbulence production and improve prediction.

This study proposes a complementary approach integrating adjoint-based data assimilation (ABDA) model and resolvent analysis to deduce the unsteady patterns of turbulent flows. For demonstration purposes, the flow behind a wall-proximity rib at two different gap-to-wall distances ( $G/d = 0.25$  and  $0.50$ ) is used. As He *et al.*<sup>24</sup> claimed,  $G/d = 0.25$  with suppressed Karman vortex shedding yielded the maximum heat transfer augmentation immediately behind the rib, along with overall improvement in surface heat removal; in contrast, the configuration with  $G/d = 0.50$  resulted in Karman vortex shedding and deteriorated the wall heat transfer. In measurements by He *et al.*,<sup>24</sup> a split-fiber probe accurately captured wall jet and flow reattachment, while the great uncertainty of PIV measurements in the high-shear regions prevented the determination of the exhaustive flow dynamics behind the rib. The same flow configuration is used in the present study, where the Reynolds number based on the free-stream velocity  $U_0$  and rib size  $d$  remains  $Re = 7600$ . In the present study, the mean streamwise velocity data determined by the split fiber are the sole observations used in the ABDA calculation, while the Fourier spectra of the streamwise velocity are used to calibrate the coefficients required in the reconstruction using the resolvent modes. Temperature sensitive paint (TSP) and PIV measurements are only involved as the reference for comparison. A stochastic approach<sup>25</sup> is used here rather than directly performing the SVD on the resolvent operator, due to its large matrix size. The energetic modes are obtained at each frequency, and the large scale structures are reconstructed using the leading resolvent modes.

## II. MATHEMATICAL FUNDAMENTALS

### A. Adjoint-based data assimilation

The formulation of the ABDA model<sup>23</sup> used to determine the mean flow fields for the resolvent analysis is reproduced

here. The basic idea of ABDA is to construct a spatially distributed function  $\beta(\mathbf{x})$  imposed on the production term to correct the model-form error.<sup>26</sup> The modified SA model<sup>27</sup> thus becomes

$$U_j \frac{\tilde{v}}{x_j} = \beta(\mathbf{x})P(\tilde{v}, \mathbf{U}) - D(\tilde{v}, \mathbf{U}) + T(\tilde{v}, \mathbf{U}), \quad (1)$$

where  $P(\tilde{v}, \mathbf{U})$ ,  $D(\tilde{v}, \mathbf{U})$ , and  $T(\tilde{v}, \mathbf{U})$  represent the production, dissipation, and transport terms of the turbulence quantity  $\tilde{v}$ , respectively. Their explicit form is given in by Spalart and Allmaras.<sup>27</sup> The dimensionless correction function  $\beta(\mathbf{x})$  changes the entire balance of the equation when it deviates from unity. Indeed, the correcting function can be added on other terms or introduced as a source term in Eq. (1). However, these make no difference in generation of the final turbulence eddy viscosity distribution, and the current formulation is typically adopted in the field inversion problem owing to the convenience in implementation. The objective of the data assimilation is achieved by minimizing the cost function  $\mathcal{J}$ , i.e., the discrepancy between the results obtained by the corrected SA model [Eq. (1)] and the observations, subject to the governing equations and the SA model. Here, the streamwise component of the velocity  $U_x$  on several straight lines inside the domain is used as the observation data. The cost function  $\mathcal{J}$  can be subsequently presented as

$$\mathcal{J} = \frac{\xi_2}{\sqrt{\xi_1}} \int_{\Omega} M \left( \frac{U_x - U_{x,\text{Exp}}}{U_{\infty}} \right)^2 d\Omega + \alpha \phi \frac{\xi_2}{\sqrt{\xi_1}} \int_{\Omega} (\beta - 1)^2 d\Omega. \quad (2)$$

Here  $\Omega$  represents the computational domain.  $\alpha$  is a dimensionless weighting coefficient specifying the relative importance of the second term in the cost function.  $\phi$  is a blending function defined as

$$\phi = 0.5 \left( 1 - \frac{\beta - 1}{|\beta - 1| + \epsilon} \right), \quad (3)$$

with a small positive constant  $\epsilon$  to prevent the denominator from becoming zero; this function is used to push the solution toward a large  $\beta$  value such that the steadiness of the primal flow is guaranteed. A masking function  $M$  is defined to specify the region where the observation data are obtained. The values of  $M$  at the cell centers close to the lines are set to unity and remain zero in other regions.  $\xi_1$  and  $\xi_2$  are dimension converters of dimensions  $[L^2]$  and  $[L^3 \cdot T^{-3}]$ , respectively, and are set to value unity to cope with the dimensional inconsistency. Following the strategy of choosing the appropriate adjoint variables to deplete the variation of the Lagrange function  $\mathcal{L}$  with respect to the state variables, i.e.,  $\delta_U \mathcal{L} + \delta_p \mathcal{L} + \delta_{\tilde{v}} \mathcal{L} = 0$ , where  $\mathcal{L} = \mathcal{J} + \int_{\Omega} (\mathbf{V}, q, \tilde{\omega}) \mathcal{R} d\Omega$ , the adjoint equation associated with the adjoint state variables  $\mathbf{V}$ ,  $q$ , and  $\tilde{\omega}$ , and the corresponding boundary conditions can be derived<sup>23,28</sup>

$$\begin{aligned} V_j \frac{\partial U_j}{\partial x_i} - U_j \frac{\partial V_i}{\partial x_j} - \frac{\partial}{\partial x_j} \left[ (\nu + \nu_t) \frac{\partial V_i}{\partial x_j} \right] + \frac{\partial q}{\partial x_i} - \frac{\tilde{v}}{\xi_1} \frac{\partial \tilde{\omega}}{\partial x_i} \\ + 2M \frac{\xi_2}{\sqrt{\xi_1}} \frac{\mathbf{U} - \mathbf{U}_{\text{Exp}}}{U_{\infty}^2} = 0, \end{aligned} \quad (4a)$$

$$\frac{\partial V_j}{\partial x_j} = 0, \quad (4b)$$

$$\begin{aligned} -U_j \frac{\partial \tilde{\omega}}{\partial x_j} - \frac{\partial}{\partial x_j} \left[ \left( \frac{\tilde{v}}{\sigma_{vt}} + \frac{\nu}{\sigma_{vt}} \right) \frac{\partial \tilde{\omega}}{\partial x_j} \right] + \frac{1 + 2C_{b2}}{\sigma_{vt}} \frac{\partial \tilde{v}}{\partial x_j} \frac{\partial \tilde{\omega}}{\partial x_j} \\ + \left( 2 \frac{C_{b2}}{\sigma_{vt}} \frac{\partial^2 \tilde{v}}{\partial x_j^2} - \beta C_{b1} \tilde{S} + 2C_{w1} f_w \frac{\tilde{v}}{d_w^2} \right) \tilde{\omega} + \xi_1 f_{v1} \frac{\partial V_i}{\partial x_j} \frac{\partial U_i}{\partial x_j} = 0. \end{aligned} \quad (4c)$$

On the inflow, wall, and far-field boundaries, the conditions are specified as follows:

$$\mathbf{V}_{\tau} = 0, \quad \mathbf{V}_n = 0, \quad (5a)$$

$$\frac{\partial q}{\partial x_i} \cdot \mathbf{n} = 0, \quad (5b)$$

$$\tilde{\omega} = 0. \quad (5c)$$

On the outflow boundaries, the conditions are specified as follows:

$$\mathbf{U}_n \cdot \mathbf{V}_{\tau} + (\nu + \nu_t) \left( \frac{\partial \mathbf{U}_{\tau}}{\partial x_i} \cdot \mathbf{n} \right) = 0, \quad (6a)$$

$$\mathbf{U}_n \cdot \mathbf{V}_n + (\nu + \nu_t) \left( \frac{\partial \mathbf{U}_n}{\partial x_i} \cdot \mathbf{n} \right) + \frac{\tilde{v} \tilde{\omega}}{\xi_1} - q = 0, \quad (6b)$$

$$\mathbf{U}_n \tilde{\omega} + \left( \frac{\tilde{v}}{\sigma_{vt}} + \frac{\nu}{\sigma_{vt}} \right) \left( \frac{\partial \tilde{\omega}}{\partial x_i} \cdot \mathbf{n} \right) - \xi_1 f_{v1} \left( V_i \frac{\partial U_i}{\partial x_j} \cdot \mathbf{n} \right) = 0. \quad (6c)$$

It should be noted in Eq. (4a) that the fluid density has been absorbed in the pressure. Equation (6a) provides a tangential component condition that is highly sensitive to the primal velocity and induces serious instability in the adjoint equations. It is thus removed, resulting in a zero-gradient condition for the adjoint velocity. During the computation, the assignments,

$$U_{y,\text{Exp}} = MU_y, \quad (7a)$$

$$U_{z,\text{Exp}} = MU_z, \quad (7b)$$

are performed at each iteration to ensure only the streamwise component of the velocity is used as the constraint. Once the adjoint state variables are obtained, the sensitivities of the Lagrange function  $\mathcal{L}$  with respect to the correcting function  $\beta$  can be computed according to

$$\frac{\partial \mathcal{L}}{\partial \beta} = 2\alpha \phi \frac{\xi_2}{\sqrt{\xi_1}} (\beta - 1) - \frac{C_{b1} \tilde{S} \tilde{\omega}}{\xi_1}. \quad (8)$$

The correction function  $\beta$  can thus be adjusted gradually to minimize the cost function using the steepest descent algorithm.<sup>29</sup>

## B. Resolvent analysis

Following McKeon and Sharma,<sup>20</sup> we consider the two-dimensional incompressible Navier-Stokes (N-S) equations

$$\frac{\partial u_i}{\partial t} + u_j \frac{\partial u_i}{\partial x_j} - \nu \frac{\partial^2 u_i}{\partial x_j^2} + \frac{\partial p}{\partial x_i} = 0, \quad (9a)$$

$$\frac{\partial u_j}{\partial x_j} = 0, \quad (9b)$$

with  $\mathbf{u}$ ,  $p$ , and  $\nu$  representing the instantaneous (primary) velocity, (primary) pressure, and viscosity, respectively. Note that the fluid density has been absorbed in the pressure. A Reynolds decomposition of the velocity and pressure around the mean flow yields the fluctuating equations

$$\frac{\partial u'_i}{\partial t} + U_j \frac{\partial u'_i}{\partial x_j} - u'_j \frac{\partial U_i}{\partial x_j} - \nu \frac{\partial^2 u'_i}{\partial x_j^2} + \frac{\partial p'}{\partial x_i} = \overline{u'_j \frac{\partial u'_i}{\partial x_j}} - u'_j \frac{\partial u'_i}{\partial x_j}, \quad (10a)$$

$$\frac{\partial u'_j}{\partial x_j} = 0, \quad (10b)$$

where  $\mathbf{U}$  represents the mean (Reynolds-averaged) velocity and the prime denotes the fluctuation. Note that no small perturbation is assumed so that Eq. (10a) is a representation of a fully nonlinear system. However, when a turbulence forcing term is defined as

$$\mathbf{f}' = u'_j \frac{\partial u'_i}{\partial x_j} - u'_j \frac{\partial u'_i}{\partial x_j}, \quad (11)$$

then Eq. (10a) can be regarded as a linear forcing-response system under a forcing  $\mathbf{f}'$  with a zero mean value. We seek the harmonic perturbation at a specific frequency  $\omega$ , yielding a form

$$\begin{bmatrix} \mathbf{u}' \\ p' \\ \mathbf{f}' \end{bmatrix} = \begin{bmatrix} \hat{\mathbf{u}} \\ \hat{p} \\ \hat{\mathbf{f}} \end{bmatrix} e^{i(\omega t + k z)} + c.c., \quad (12)$$

with “c.c.” indicating the conjugate complex of the perturbation. Only a two-dimensional perturbation is considered presently with spanwise wavenumber  $k = 0$ . Doing so enables the easy transformation of this forcing-response system to the Fourier space as

$$\hat{\boldsymbol{\psi}} = (\mathbf{A} + \omega \mathbf{B})^{-1} \mathbf{P} \hat{\mathbf{f}}, \quad (13)$$

where

$$\mathbf{A} = \begin{bmatrix} U_x \frac{\partial}{\partial x} + U_y \frac{\partial}{\partial y} + \left( \frac{\partial}{\partial x} + \frac{\partial}{\partial y} \right) U_x - \nu \left( \frac{\partial^2}{\partial x^2} + \frac{\partial^2}{\partial y^2} \right), & 0, & \frac{\partial}{\partial x} \\ 0, & U_x \frac{\partial}{\partial x} + U_y \frac{\partial}{\partial y} + \left( \frac{\partial}{\partial x} + \frac{\partial}{\partial y} \right) U_y - \nu \left( \frac{\partial^2}{\partial x^2} + \frac{\partial^2}{\partial y^2} \right), & \frac{\partial}{\partial y} \\ & \frac{\partial}{\partial x}, & \frac{\partial}{\partial y}, & 0 \end{bmatrix}, \quad (14)$$

$$\mathbf{B} = \begin{bmatrix} i, 0, 0 \\ 0, i, 0 \\ 0, 0, 0 \end{bmatrix}, \quad \mathbf{P} = \begin{bmatrix} 1, 0, 0 \\ 0, 1, 0 \\ 0, 0, 0 \end{bmatrix}, \quad \hat{\boldsymbol{\psi}} = \begin{bmatrix} \hat{\mathbf{u}} \\ \hat{p} \end{bmatrix}.$$

Define the resolvent operator as

$$\mathcal{R}(\omega) = (\mathbf{A} + \omega \mathbf{B})^{-1} \mathbf{P}, \quad (15)$$

which serves as the transfer function from the forcing  $\hat{\mathbf{f}}$  to the flow response  $\hat{\boldsymbol{\psi}}$ . At each frequency, the dynamic properties can be analyzed by the singular value decomposition (SVD) of the resolvent operator.<sup>20,21</sup> The resultant right eigenvectors denote the spatial patterns of the optimal forcing that give the most energetic flow responses, while the left eigenvectors represent the optimal flow responses, which are called resolvent modes  $\hat{\boldsymbol{\phi}}$ ; the response energy can be seen from the eigenvalues.

In Eq. (14),  $\mathbf{A}$  and  $\mathbf{B}$  are large matrices that depend on the number of the state variables and the degree-of-freedom of the flow system, which leads to great difficulties in the matrix inversion in Eq. (15) and the SVD decomposition. Dergham *et al.*<sup>30</sup> spent almost 15 h on a workstation with 440 processors and more than 800 GB memory to solve the SVD of a matrix of size  $10^5 \times 10^5$ . In fact, simple two-dimensional flows will yield this matrix size, while three-dimensional analysis is currently impossible. Here, a stochastic approach<sup>25</sup> is adopted, which significantly decreases the matrix size and enables computation on a conventional desktop. This approach involves imposing a white-noise forcing at a specified frequency on the system [Eq. (13)] before performing proper orthogonal decomposition (POD)<sup>31</sup> on the cross-spectral density matrix. The POD eigenmodes (called resolvent modes, which are distinct from the conventional POD model applied to the PIV result) correspond to the optimal responses of the flow system, while the eigenvalues denote the energies of the resolvent modes. This strategy reduces the computation cost in two ways: it avoids the matrix inversion in Eq. (15) and decreases the matrix size to  $N \times N$  ( $N$  is the number of the stochastic forcing) when the snapshot method<sup>32</sup> is used.

The resolvent analysis provides optimal responses which are orthogonal in space. Generally speaking, once a full rank of the responses is obtained, they can be used to completely reconstruct the Fourier mode at this frequency given the coefficients. However, these coefficients in the reconstruction are distinct from the POD coefficients in the stochastic resolvent analysis. A commonly used method is the calibration of the coefficient only for the leading resolvent mode using the spectra of the pointwise measurement data,<sup>6,22</sup> as it has been noted that the leading resolvent mode is enough for the reconstruction when the flow is convectively unstable. For more complex flows where the unsteadiness is governed by different instability mechanisms, such as the present flow over a wall-proximity rib, we note that reconstruction using the resolvent modes is still feasible, except that more modes must be considered. Using the first  $n$  resolvent modes  $\hat{\boldsymbol{\phi}}$ , the calibration and reconstruction can be expressed as

$$\mathbf{u} = \sum_{i=1}^n c_i \hat{\boldsymbol{\phi}}_i. \quad (16)$$

In calibration,  $c$  can be determined using multiple pointwise observational data in terms of least squares, while the spatial pattern of the flow unsteadiness can be reconstructed using the resultant coefficients.

### III. COMPUTATIONAL AND EXPERIMENTAL SETUP

#### A. Computational setup

The computational domain studied here is two-dimensional and is based on our previous measurements<sup>24</sup> so as to make use of the experimental data. As shown in Fig. 1, the rib size is  $d = 10$  mm, and it is located  $15d$  downstream of the inflow boundary. The height of the domain is  $15d$  so that the effect of the far-field boundary can be neglected. The domain length of  $56d$  is used to eliminate the effects of the outflow

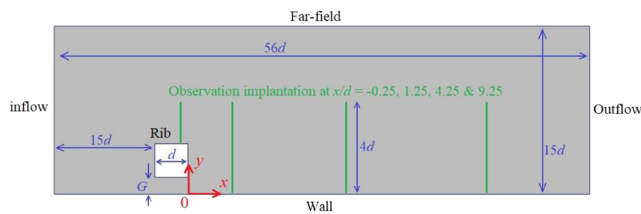


**FIG. 1.** Schematic of the computational domain. The green lines represent the implantation location of the observational data.

boundary on the computation. For both cases of  $G/d = 0.25$  and  $0.5$ , structured grids with  $0.13 \times 10^6$  cells are used, which are sufficient to fulfill the grid-independent criterion.

The data assimilation is performed using the open-source code OpenFOAM (<http://openfoam.org>). For the primary state variables, the inflow boundary condition is obtained by a precursor SA simulation for the flat plate with the boundary layer thickness of  $2d$  at the inflow boundary location, which is consistent with the split fiber measurement.<sup>24</sup> The no-slip condition is imposed on the rib surface and wall, while the free-slip condition is used for the far-field boundary. The zero-gradient condition is applied on the outflow boundary. All the boundary conditions of the adjoint variables are imposed according to the discussion in Sec. II A. For each configuration, the split fiber data (to be discussed in Sec. III B) at  $x/d = -0.25, 1.25, 4.25,$  and  $9.25$ , and  $0 < y/d < 4$  are used as the observations with the streamwise velocity constraint and are located in the centers of the nearest cells. The convection terms in all the primal equations are discretized using a linear-upwind scheme which is derived from the upwind scheme and returns upwind weighting factors with an explicit correction to achieve boundedness and second-order accuracy, while the first-order upwind is used for the adjoint equations to increase numerical stability.  $\alpha$  is set to  $1 \times 10^{-6}$  for the case of  $G/d = 0.25$  to eliminate any constraint on the  $\beta$  determination, while  $\alpha = 1 \times 10^{-2}$  for the case of  $G/d = 0.50$  to push the result toward larger  $\beta$  values, as otherwise negative  $\beta$  and flow instability occur in this configuration. It should be noted that heat transfer is not considered in the assimilation because the current eddy viscosity is only optimized for turbulence flows. Heat transfer data assimilation requires a new optimization process that is beyond the scope of the present study.

In resolvent analysis, matrices  $A$  and  $B$  are computed using the finite-element-based FreeFem++ code (<http://www.freefem.org/>). 1000 samples of the white-noise forcing at Strouhal numbers  $St = 0.02, 0.05, 0.15,$  and  $0.30$  are imposed to calculate the stochastic flow response; in fact, a sample-independent test has shown that 500 samples are enough for the resolvent analysis convergence. The resolvent modes are obtained using the snapshot POD method applied on the cross-spectral density matrices.<sup>25</sup> At  $St = 0.15$ , Fourier spectra in the band  $St \pm 0.01$  are summed by taking the norms of the real and imaginary parts, before the reconstruction coefficients are calibrated using the summed Fourier spectra obtained by the split fiber at  $x/d = 1.25, 4.25,$  and  $9.25$

and  $y/d = 0.2, 0.4, 1,$  and  $1.4$ ; the reason is that these resolvent modes in the frequency band represent the same spatial structures.

## B. Experimental setup

A detailed description of the experiment has been provided in our previous work,<sup>24</sup> and thus only a brief account is given here. A plexiglas square rib with size  $d = 10$  mm was used in the measurement and was placed at the leading edge of the heat area. The flow and heat transfer measurements were performed separately without and with heating on the target surface. Only the data at  $G/d = 0.25$  and  $0.50$  at Reynolds number  $Re = 7600$  are used in the analysis and compared with the present study. In the heat transfer experiment, the two-dimensional wall temperature distribution behind the rib was measured by TSP. The normalized Nusselt number distribution  $\widehat{Nu}$  was time and spanwise averaged to determine the heat transfer enhancement with respect to the flat plate boundary layer, where  $\widehat{Nu}$  was expressed as

$$\widehat{Nu} = \frac{Nu - Nu_0}{Nu_0}. \quad (17)$$

Here,  $Nu_0$  is the time and spanwise averaged Nusselt number on the flat plate without the rib determined by the same measurement system. The turbulent flow on the streamwise vertical-center plane behind the rib was measured using PIV at the sampling rate 1 Hz. As a complementary method for flow measurement, a split-fiber film probe was used to survey the highly unsteady wake with flow reversal at sampling rate 5 kHz. Measurement was performed along the wall-normal direction at four locations,  $x/d = -0.25, 1.25, 4.25,$  and  $9.25$ . The split fiber determined a boundary layer thickness of  $\delta = 2d$  at a location  $15d$  upstream of the rib, which was the reference for specification of the inflow boundary layer in the data assimilation.

Because PIV aimed to capture the global patterns of the turbulent flow behind the rib, the spatial resolution was limited, giving rise to substantial error in the strong shear layer.<sup>24</sup> In the framework of the present study, only the split fiber results are required as observational data in the data assimilation and in the resolvent analysis for coefficient calibration. The TSP and PIV results, however, are used as complementary data for flow and heat transfer analysis.

## IV. RESULTS AND DISCUSSION

### A. Data assimilation of the flows

Figures 2 and 3 present the data assimilation result of the flow at  $G/d = 0.25$  and  $0.50$ , respectively. The time and spanwise averaged  $\widehat{Nu}$  distribution is shown in Figs. 2(a) and 3(a) for ease of discussion. Figures 2(b) and 3(b) compare the streamwise velocity distribution at  $x/d = -0.25, 1.25, 4.25,$  and  $9.25$  determined by the split fiber, PIV, the default SA model simulation, and the ABDA model. The inaccuracy of the PIV measurement at  $x/d = -0.25$  and  $1.25$  for both cases is significant, which is induced by the spatial resolution of the camera

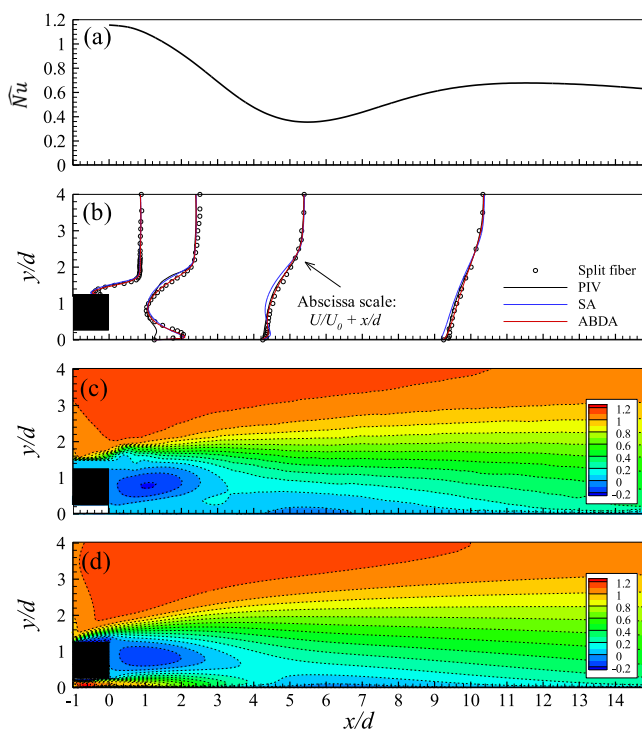


**FIG. 2.** Normalized Nusselt number and flow fields at  $G/d = 0.25$ . (a) Time and spanwise averaged normalized Nusselt number distribution on the heated wall measured by TSP. (b) Comparison of the mean streamwise velocity at  $x/d = -0.25, 1.25, 4.25$ , and  $9.25$  determined by split fiber, PIV, SA model, and ABDA. (c) Mean streamwise velocity distribution determined by PIV. (d) Mean streamwise velocity distribution determined by ABDA.

and has been discussed in detail by He *et al.*<sup>24</sup> In fact, PIV is still a very good means of flow field measurement in various flow conditions; the present inaccuracy can be solved by zooming in the camera in a small region behind the rib. However, there is a tradeoff between the flow field resolution and the extent of the global flow region. For the subsequent resolvent analysis, an accurate global flow field with an adequate spatial extent is critical for the calculation of the forcing-response system [Eq. (13)]. Therefore, the PIV results cannot meet the requirement because of this inaccuracy and the lack of flow data below the rib due to the shadow. While the SA simulation shows significant discrepancy with the split fiber results in both cases, the ABDA results show good agreement both in the upper shear layer and the lower wall-jet region. These results demonstrate the practicability of the ABDA model in the prediction of complex flows. The global patterns of the mean streamwise velocities determined by PIV and the ABDA model are presented in Figs. 2(c), 2(d), 3(c), and 3(d) for both cases. A significant improvement of the flow fields is obtained by the ABDA model in the separation region above the rib, in the recirculation bubble, and in the wall-jet region, while little difference can be observed at  $x/d > 5$ .

Given that accurate flow fields have been obtained for both cases, the heat transfer properties on the wall can be

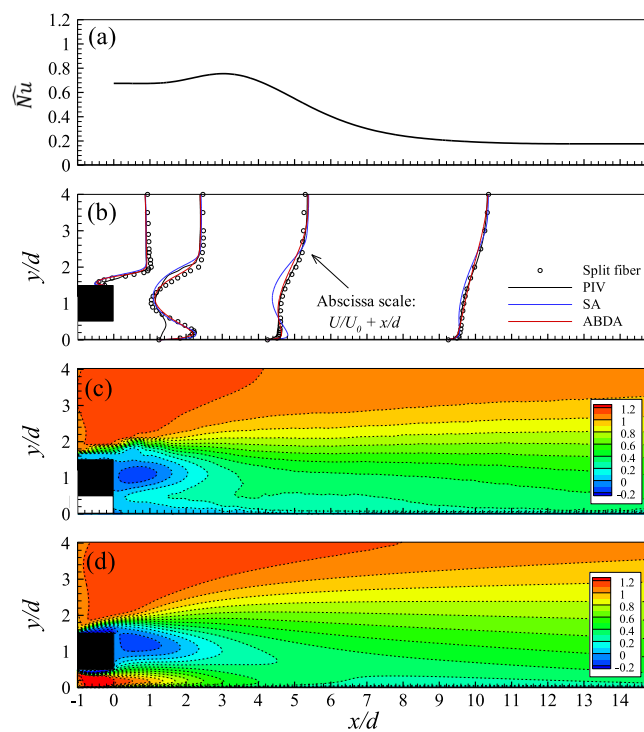


**FIG. 3.** Normalized Nusselt number and flow fields at  $G/d = 0.50$ . (a) Time and spanwise averaged normalized Nusselt number distribution on the heated wall measured by TSP. (b) Comparison of the mean streamwise velocity at  $x/d = -0.25, 1.25, 4.25$ , and  $9.25$  determined by split fiber, PIV, SA model, and ABDA. (c) Mean streamwise velocity distribution determined by PIV. (d) Mean streamwise velocity distribution determined by ABDA.

analyzed. In the case of  $G/d = 0.25$ , the heat transfer in the region immediately behind the rib is substantially enhanced by the wall-jet originating from the gap, as shown in Figs. 2(a) and 2(d). The normalized Nusselt number decays in the downstream direction with the attenuation of the wall jet velocity. A boundary layer separation can be observed at  $x/d = 5$  [Fig. 2(d)], resulting in the lowest level of heat transfer intensity. In the case of  $G/d = 0.50$ , the heat transfer intensity immediately behind the rib is lower than that at  $G/d = 0.25$ . This decrease partially results from the velocity gradient decrease in the wall jet, indicated by the sparser velocity contour in Fig. 3(d) than in Fig. 2(d). Another reason is the lack of energetic structures in the wall jet at  $G/d = 0.50$ , as is shown in more detail in Figs. 8 and 10. The wall jet ends at  $x/d = 4$ , where the heat transfer intensity begins to decay, as shown in Fig. 3(a).

The flow prediction augmentation in the ABDA model is achieved by modification of the eddy viscosity distribution. Doing so, however, does not give any direct link to the wall heat transfer prediction using the same model. For the conventional heat transfer prediction, the turbulent heat transfer model is based on the turbulent thermal diffusivity, which is calculated using the ratio between the eddy viscosity and turbulent Prandtl number. The turbulent Prandtl number is

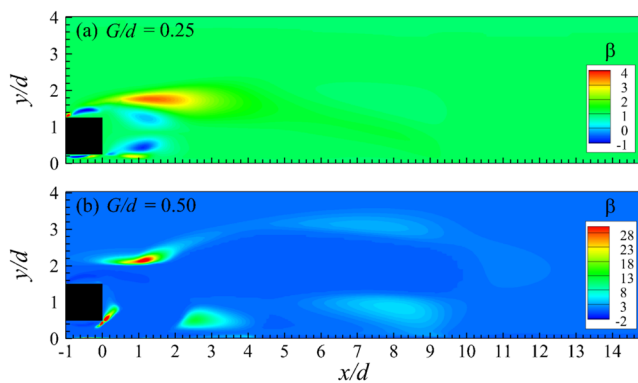


FIG. 4. Correction coefficient  $\beta$  distribution for different cases.

usually assumed to be a constant. As shown in Fig. 4, the correction coefficient  $\beta$  in these two cases has significantly different values and distributions, even though the geometries are topologically similar. This variation indicates the infeasibility of heat transfer assimilation directly using the modified eddy viscosity, and hence the heat transfer is not involved in the present data assimilation and resolvent analysis. Nevertheless, the development of the assimilation model for heat transfer is beyond the scope of the present study.

## B. Experimental results and analysis

Figures 5 and 6 present the POD results based on the PIV measurement; these figures have been reported in our previous work,<sup>24</sup> where detailed discussion can be found. They are recalled here to demonstrate the flow dynamics in these specific flow configurations. Figure 5 displays the eigenvalues of the leading 10 POD modes, which represents the relative contribution of the POD modes to the total fluctuation energy. The significant difference is that the mode energy for the case

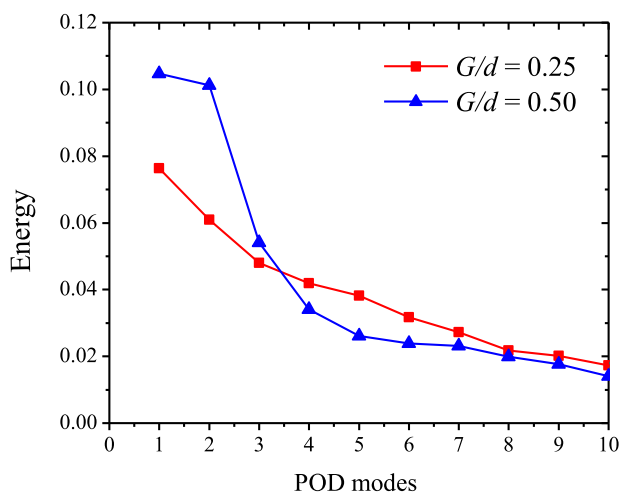


FIG. 5. Normalized energy of the POD models (PIV measurement).

of  $G/d = 0.25$  decays consistently toward higher order, while the energy of the first two modes in the case of  $G/d = 0.50$  is comparable and is notably higher than others. In the latter configuration, the unsteady flow is overwhelmingly dominated by the first pair of POD modes, indicating the existence of Karman-vortex-like convective structures in the wake region.

The POD modes of the two cases, presented by the vertical component of the normalized velocity (normalized by the norm of corresponding mode vector), are shown in Fig. 6. For the case of  $G/d = 0.25$  [Fig. 6(a)], we previously provided the explanation that the first two POD modes represented the flapping motion of the separation bubble close to the surface, while the third and fourth POD modes indicated the second pair of structures, which were coupled to represent the convective motion of the dominant vortical structures.<sup>24</sup> However, the coupling of the first two and second two POD modes (Karman-vortex-like structures) was not sufficiently evidenced. The understanding and interpretation of these structures can be corrected using the present resolvent analysis, which is presented in Figs. 9 and 14. In the configuration with  $G/d = 0.50$  [Fig. 6(b)], the first two POD modes included a readily recognized Karman vortex street. It was distinctively different from the other two configurations, in which the flapping motion of the separation bubble made the primary contribution to the total fluctuation energy. In addition, the third and fourth POD modes exhibited features similar to those in the case of  $G/d = 0.25$  in connection with the flapping motion, which had much lower intensity than the Karman vortex shedding.

The power spectra densities (PSD) of the streamwise velocity measured by the split fiber at  $x/d = 1.25, 4.25,$  and  $9.25,$   $y/d = 0.2$  and  $1.0$  for both cases are presented in Fig. 7. For the case of  $G/d = 0.25$ , a slight peak of the spectra is observed at  $St = 0.15$  and  $x/d = 1.25, y/d = 0.2$  [Fig. 7(a)]; it is obviously induced by the oscillation of the wall jet. Otherwise, no significant spectral peak can be found. For the case of  $G/d = 0.50$ , a significant peak at  $St = 0.15$  or  $0.30$  (or both with light decay of  $St$  with the downstream distance) can be observed at each location. It can easily be considered the Karman vortex shedding and higher order harmonics without further evidence. However, this interpretation cannot explain the absence of the fundamental frequency at  $x/d = 1.25$  and  $y/d = 1.0$ ; this issue is presented in Fig. 11. In addition, another interesting feature of the PSD is that the case of  $G/d = 0.25$  exhibits significantly higher power in the low frequency region and lower power in the high frequency region than the case of  $G/d = 0.50$ . This feature is important for discussion of the relative strength of different resolvent modes.

## C. Resolvent analysis

Due to the broad-band feature of the flow spectra, the resolvent analysis is performed at  $St = 0.02, 0.05, 0.15,$  and  $0.30$ . The frequencies are selected based on the PSD peaks with two lower frequencies to explore the large-scale flapping motion. The energies of the resolvent modes at each frequency in the case of  $G/d = 0.25$  are presented in Fig. 8.

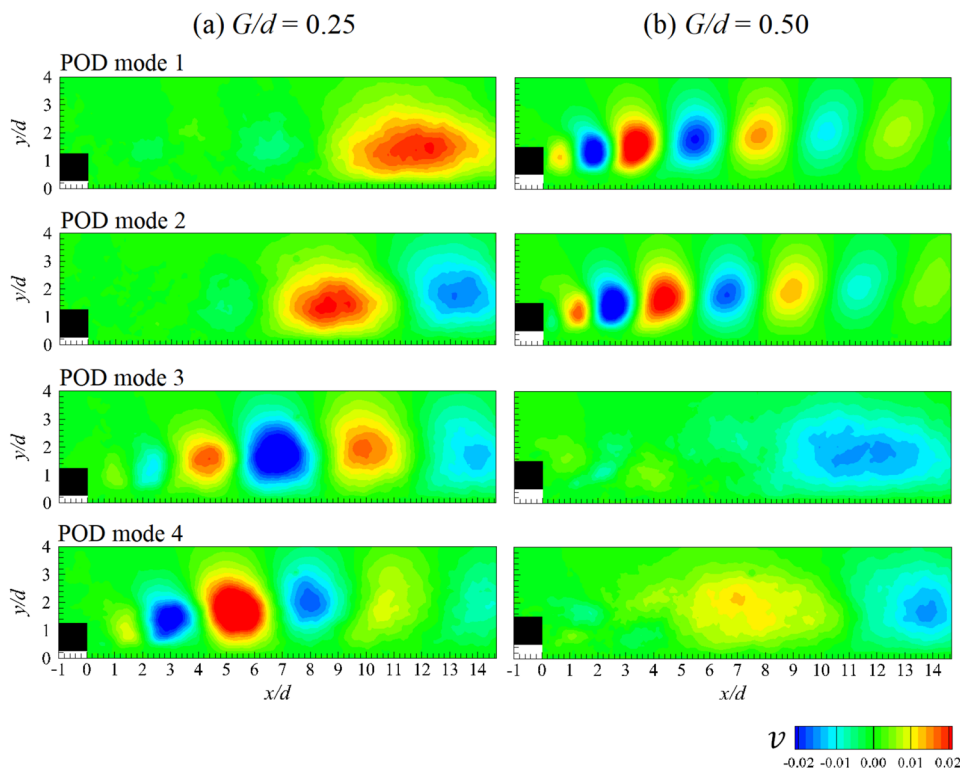


FIG. 6. Spatial distribution of the first four POD modes (PIV measurement).

It is noteworthy that the logarithmic ordinate is used so that the energy decays much faster for higher order resolvent modes than in the POD analysis (Fig. 5). Beneddine *et al.*<sup>21</sup> noted that if the flow is monochromatic at a particular frequency, the resolvent operator [Eq. (15)] would display a very strong response in the vicinity of this frequency. This response led to a clear separation of the leading resolvent mode from others in terms of energy (eigenvalue). Clearly, the leading mode is not well separated from the higher order modes in the present broad-band flows, in particular at  $St = 0.02$ ,  $0.05$ , and  $0.30$ . Due to the insignificant peak in the spectra [Fig. 7(a)], the energy at  $St = 0.15$  exhibits slightly faster decay. However, the present results suggest that the flow reconstruction using only the leading resolvent mode is not enough.

The leading resolvent mode at each frequency for the case of  $G/d = 0.25$  is presented in Fig. 9. The large-scale flapping motion can be observed at the lower frequencies  $St = 0.02$  and  $0.05$ . However, these are not distinct flow structures appearing at particular frequencies. When considering the resolvent modes at  $St = 0.15$  and  $0.30$ , we can interpret them as similar structures with the streamwise wavelength decreasing as the frequency increases. Accordingly, the flow dynamics switch gradually from large-scale flapping in the far-downstream region toward shear layer oscillation close to the upper edge of the rib. In fact, they all originate from the shear layer instability, where the vortices scale with the shear layer thickness and the frequency decays in the

streamwise direction. A similar phenomenon is indicated by the POD modes shown in Fig. 6(a), with decreasing sizes of vortical structures for the higher order POD modes. At  $St = 0.15$ , however, a sequence of oscillating structures can be observed in the region  $1 < x/d < 5$  near the wall [Fig. 9(c)], indicating the dynamical behaviors of the wall jet, which would play a beneficial role in heat removal. This behavior can also be interpreted as the suppression of Karman vortex shedding due to the small gap ratio  $G/d$ ; aside from this particular  $St$  value, another clear sign of suppression is the tendency toward Karman vortex formation that can be found at  $1 < x/d < 2$ , where the streamwise wavelength of this wall-jet oscillation is close to that of the upper shear layer. This dynamic behavior of the wall jet was absent in the PIV measurement<sup>24</sup> due to substantial error in the wall jet region. This result also suggests the ability of the present resolvent analysis to capture the fine scale dynamics that are important in turbulence flows. Recalling the PSD spectra (Fig. 7), which show significant higher power for low frequency vortices, we can draw the conclusion that the large-scale flapping motion in Figs. 9(a) and 9(b) dominates the flow, which enhances wall heat transfer in the region of the flow reattachment and agrees well with the TSP measurements and POD analysis [Fig. 6(a)]. This finding again suggests the ability of resolvent analysis to capture the dominant flow features.

The energies of the resolvent modes at each frequency in the case of  $G/d = 0.50$  are presented in Fig. 10. Different from the case of  $G/d = 0.25$ , the resolvent modes at

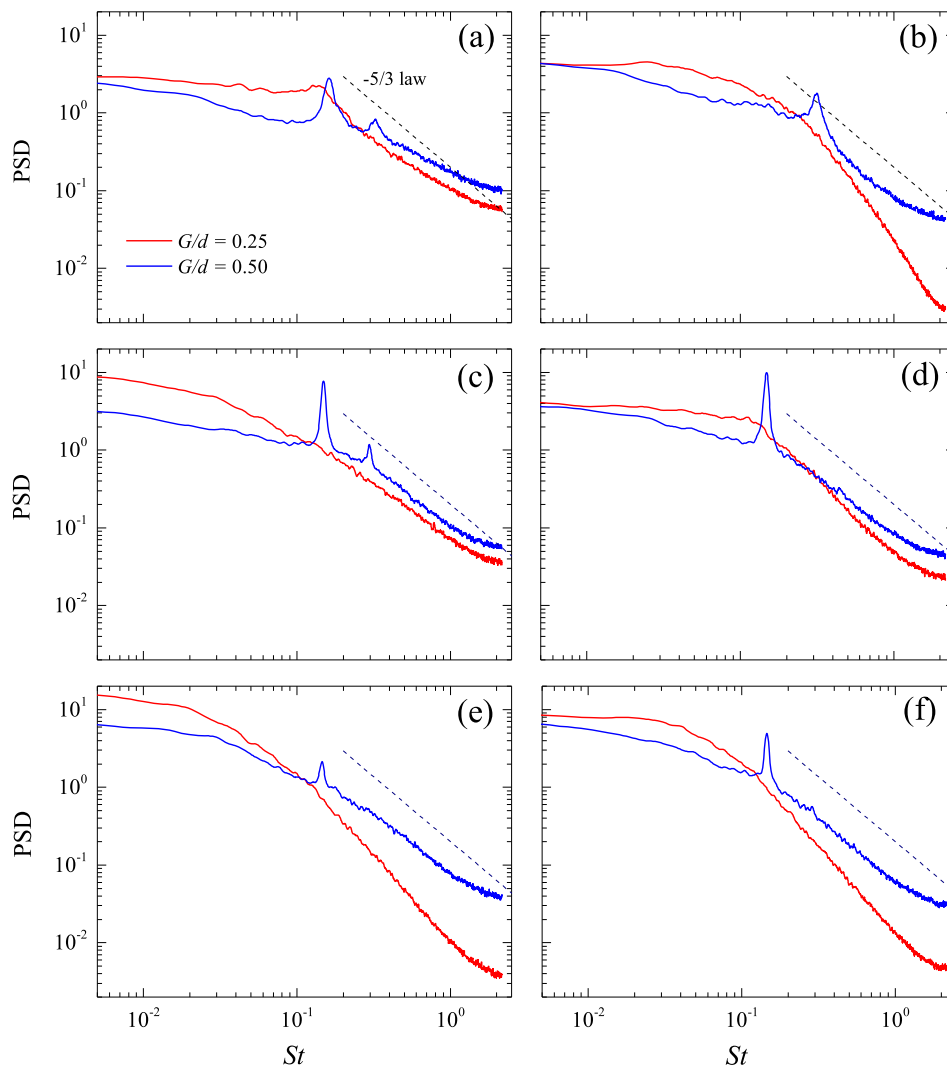


**FIG. 7.** Power spectral density of the streamwise velocity measured by split-fiber. (a)  $x/d = 1.25$  and  $y/d = 0.2$ , (b)  $x/d = 1.25$  and  $y/d = 1.0$ , (c)  $x/d = 4.25$  and  $y/d = 0.2$ , (d)  $x/d = 4.25$  and  $y/d = 1.0$ , (e)  $x/d = 9.25$  and  $y/d = 0.2$ , and (f)  $x/d = 9.25$  and  $y/d = 1.0$ .

both  $St = 0.15$  and  $0.30$  at the present gap ratio exhibit dramatic decay for higher order modes. As indicated by the PSD spectra (Fig. 7), which shows dominant power at these two frequencies, the rapid decay of the resolvent energy for higher order modes is expected according to the discussion of Beneddine *et al.*<sup>21</sup> However, the resolvent modes at  $St = 0.02$  and  $0.05$  are not well separated, which is similar to the case of  $G/d = 0.25$ . This lack of separation also induces difficulties for reconstruction at these low frequencies.

Figure 11 presents the leading resolvent mode for each frequency at  $G/d = 0.50$ . The large-scale flapping motion is also observed at  $St = 0.02$  and  $0.05$  [Figs. 11(a) and 11(b)], which is similar to the case of  $G/d = 0.25$ . However, a Karman-vortex-like structure for the leading resolvent mode at  $St = 0.15$  [Fig. 11(c)] and its harmonic at  $St = 0.30$  [Fig. 11(d)] is established. Note that the harmonic appears only in the upper shear layer, being similar to the shear layer instability. Due to the confinement of the wall, the lower part of the shear layer

instability is suppressed to some extent, as is shown in more detail in Fig. 12. According to the PSD spectra in Fig. 7(b), this shear layer instability (or harmonic) makes an overwhelming contribution to the flow dynamics locally near  $x/d = 1.25$  and  $y/d = 1.0$ , giving rise to a significant PSD peak at  $St = 0.30$ . In addition, the Karman vortex shedding, i.e., the resolvent mode at  $St = 0.15$  [Fig. 11(c)] and  $St = 0.30$  [Fig. 11(d)], dominates the flow dynamical behavior, while the large-scale flapping motion has significantly lower power than at  $G/d = 0.25$ . This result provides clear evidence for the wall heat transfer decay at  $x/d > 4$  [Fig. 3(a)], which agrees with the POD analysis [Fig. 6(b)].

The preceding discussion is based on the lead resolvent mode, which is assumed to play a dominant role in the flow dynamical behavior. Such is the case when the leading mode energy is well separated from that of the higher order modes, and the turbulent forcing [Eq. (11)] has no preferential direction toward any suboptimal forcings.<sup>21</sup> The second hypothesis usually holds for flow with significantly convective stability.

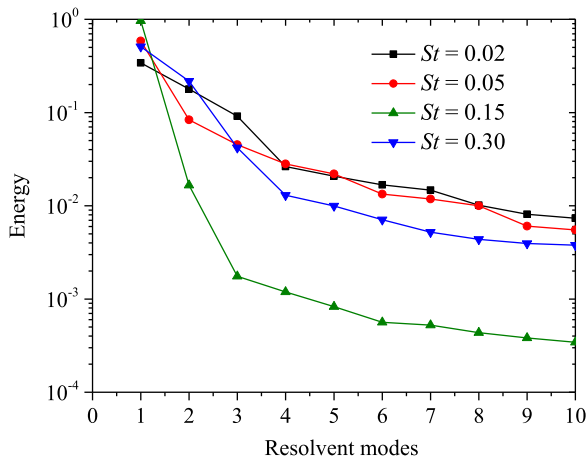


FIG. 8. Normalized energy of the resolvent models for different Strouhal numbers at  $G/d = 0.25$ .

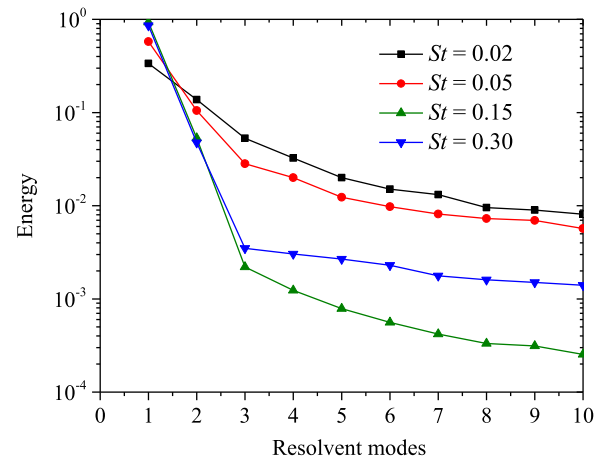


FIG. 10. Normalized energy of the resolvent models for different Strouhal numbers at  $G/d = 0.50$ .

For the flows in the present study, however, it is important to consider the contribution of the higher resolvent modes. The leading 10 resolvent modes at  $St = 0.02$  and  $0.05$  for both cases have been carefully checked, showing similar structures that are all representative of the large-scale flapping motion (not shown). The second and third resolvent modes at  $St = 0.15$  and  $0.30$  for both cases are presented in Fig. 12. For the case of  $G/d = 0.25$  [Fig. 2(a)], similar dynamical features are contained in the leading three resolvent modes with only slight

differences in spatial patterns. This result validates the previous discussion based solely on the leading mode. The second and third resolvent modes at  $St = 0.30$  for  $G/d = 0.25$  indicate the existence of the up-down oscillation of the wall jet. The wall jet separation can be observed from the departure of the model structures away from the wall at approximately  $x/d = 5$ . For the case of  $G/d = 0.50$ , the second and third resolvent modes at  $St = 0.15$  also represent the Karman vortex shedding with slight spatial difference. This result suggests

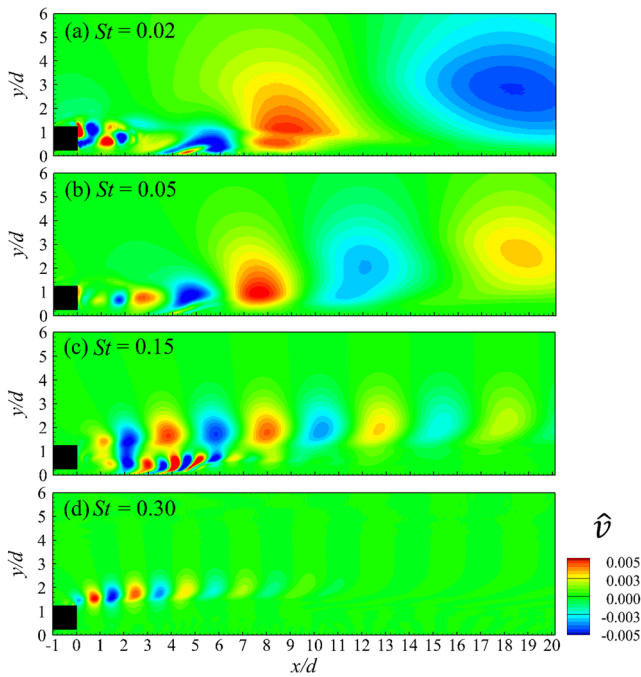


FIG. 9. Spatial distribution of the first resolvent model for different Strouhal numbers at  $G/d = 0.25$ .

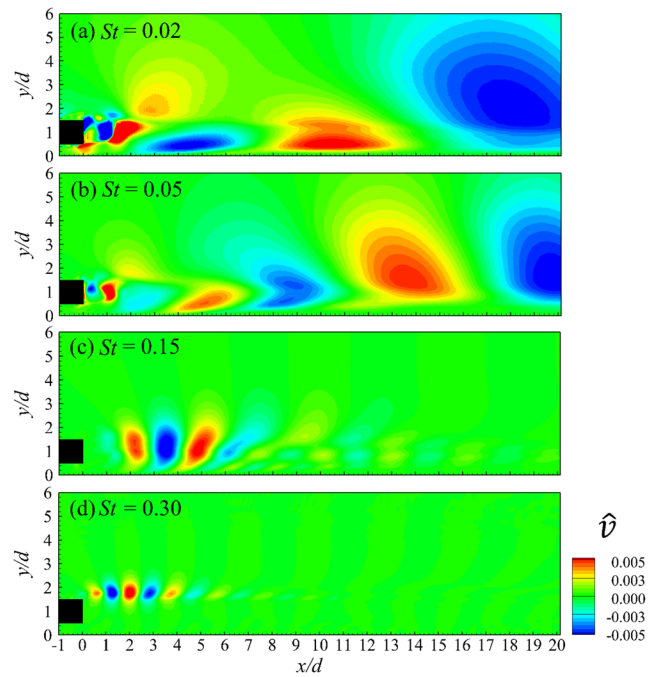


FIG. 11. Spatial distribution of the first resolvent model for different Strouhal numbers at  $G/d = 0.50$ .

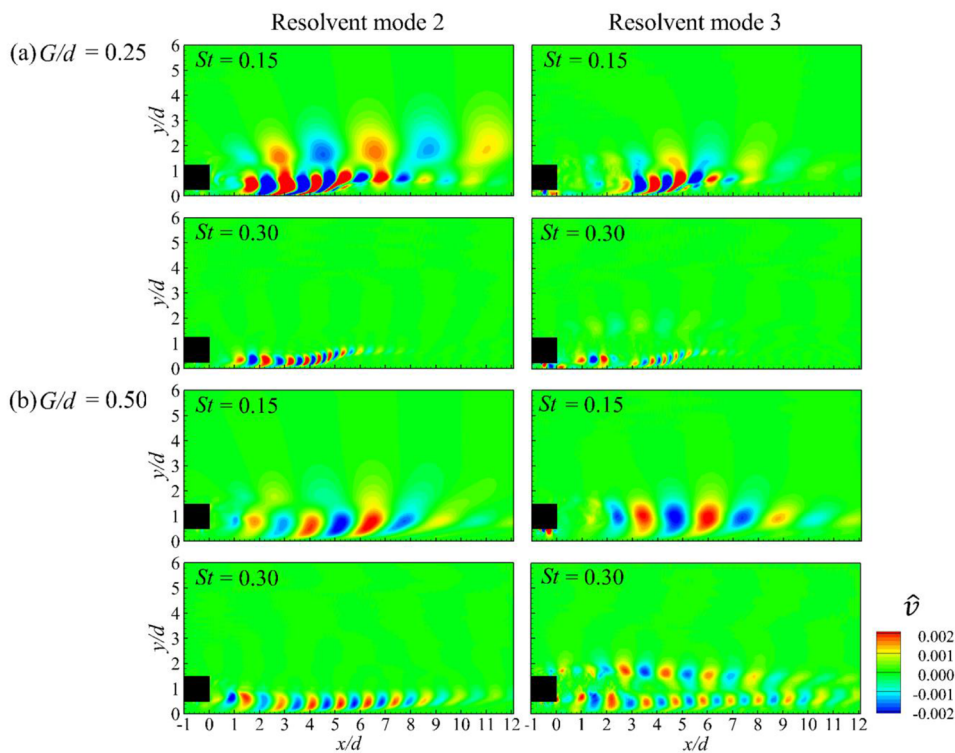


FIG. 12. Spatial distribution of the second and third resolvent modes for different Strouhal numbers.

that reconstruction solely using the leading resolvent mode is incorrect when the higher order modes contribute. At  $St = 0.30$ , the wall jet oscillation is present in the second resolvent mode, while in the third mode, the harmonic of the Karman vortex shedding is observed. This result clearly indicates that a single flow dynamical structure is not well separated by the resolvent modes. The further higher order resolvent modes are not presented here, as they have no distinct difference in physical interpretation, except for a slight difference in spatial distribution.

In short, the reconstruction of the flow dynamics is not straightforward in the present study. The main difficulty is the unknown contribution made by each resolvent mode at a specified frequency. The rank-1 approximation used by Beneddine *et al.*<sup>21</sup> is indeed not valid. However, we must still consider the hypothesis that turbulent forcing has no preferential direction toward any suboptimal forcings (right eigenvectors of the SVD of the resolvent operator matrix); in other words, the true turbulence forcing expressed by Eq. (11) has projections on each right eigenvector in the same order. Therefore, the true forcing components in the direction of the low order optimal forcings induce strong flow responses that dominate the flow dynamical behavior. Thus, the flow can be reconstructed using several leading resolvent modes obtained at a specified frequency, using coefficients calibrated by the Fourier spectra of the split fiber measurements. For both cases, the Fourier spectra at 12 locations, i.e.,  $x/d = 1.25, 4.25, \text{ and } 9.25$ ,  $y/d = 0.2, 0.4, 1.0, \text{ and } 1.4$ , are used to calibrate the coefficients in Eq. (16) in a least square manner. Only

$St = 0.15$  is considered presently for demonstration purposes. Due to the uncertainty of the Fourier spectral computation, the spectral norms of the real and imaginary parts in the band  $0.14 < St < 0.16$  are considered, which contains the contributions of all turbulent fluctuations in  $0.14 < St < 0.16$ , assuming the spatial patterns of the resolvent modes are identical with that at  $St = 0.15$ . Using different numbers of resolvent modes, the calibrated coefficients for the cases of  $G/d = 0.25$  and  $0.50$  are presented in Fig. 13. It can be seen at  $G/d = 0.25$  [Fig. 12(a)] that the coefficients of the first two resolvent modes converge when the first five resolvent modes are used for calibration and reconstruction. However, a further increase in the number of resolvent modes induces anomalies even for coefficients of the first two modes. Beneddine *et al.*<sup>21</sup> demonstrated that the selection of observational data is important and that they should be located in the high-energy region. Using higher order modes induces low-energy regions in which the observational data are located, limiting the number of modes that can be used in calibration. Fortunately, it is shown in Figs. 14 and 16 that even though several coefficients do not converge well, the main features of the reconstructed fields do not change with the increasing number of resolvent modes. For the case of  $G/d = 0.50$ , the coefficients of the first two resolvent modes also converge well using the first five resolvent modes for reconstruction. Nevertheless, the five coefficients are determined reasonably well, as is demonstrated in Fig. 16.

The reconstructed fields at  $St = 0.15$  for the case of  $G/d = 0.25$  are presented in Fig. 14. Note that the mean flow is not used in the reconstruction so that it can be compared

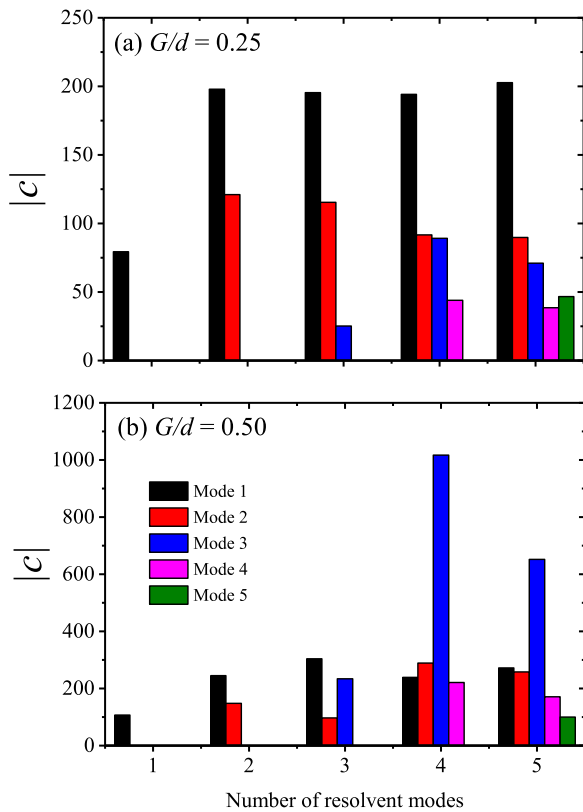


FIG. 13. Norms of the resolvent coefficient when reconstructed using different numbers of resolvent modes.

with the POD mode and the POD mode is renormalized to be comparable with the reconstructed field. Because the POD mode contains different frequency components, its amplitude cannot be compared with the reconstruction direction. Only the spatial pattern is considered here. It shows that the reconstruction pattern converges when more than two resolvent modes are used. Using five resolvent modes yields some fine scales near the wall jet region. It can be observed that the streamwise wavelength of the reconstructed structure remains slightly smaller than that of the POD mode. One reason is that the POD mode captures the most energetic structures within the whole frequency band, while the energetic frequency is significantly lower than  $St = 0.15$ . The structures with larger wavelengths are thus contained in the POD mode. The fine scale distribution reconstructed using the first five resolvent modes is presented in Fig. 15 in terms of vorticity. The wall jet oscillation can be observed at  $x/d < 4$  with the separation at  $x/d = 5$ , giving rise to substantial heat transfer enhancement immediately behind the rib and thus the minimum heat transfer at  $x/d = 5$ .

The reconstructed fields at  $St = 0.15$  for the case of  $G/d = 0.50$  are presented in Fig. 16. The structure changes slightly in the region  $x/d > 7$  when the mode number increases from 2 to 5, which can be attributed to the nonconvergent coefficients for high order resolvent modes. However, the

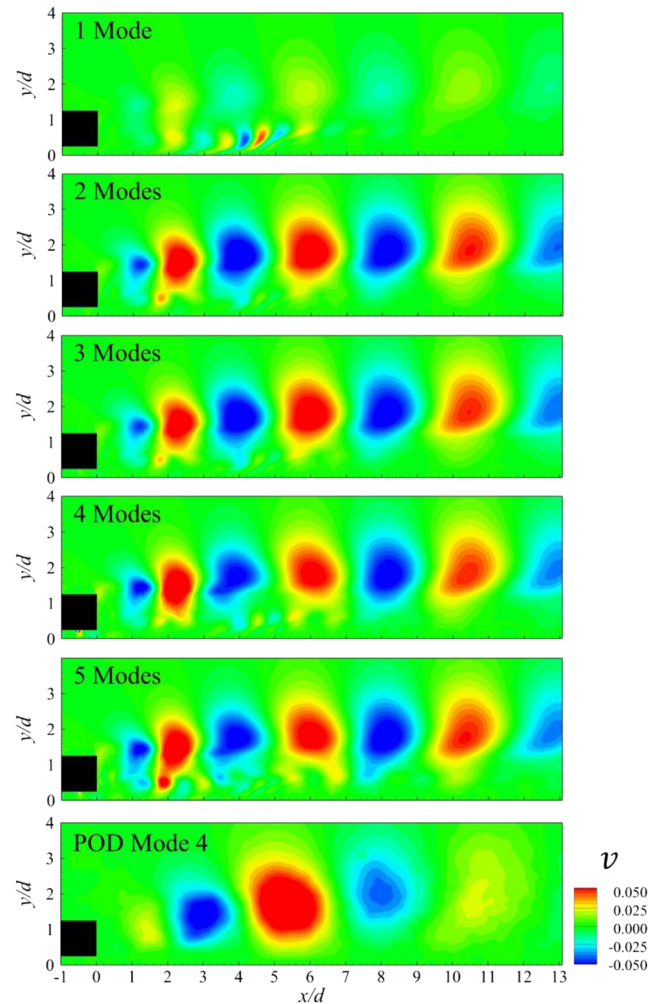


FIG. 14. Reconstructed fields using different numbers of resolvent modes at  $St = 0.15$  and  $G/d = 0.25$  and comparison with the POD mode.

reconstructed pattern has much better agreement with that of the POD mode than at  $G/d = 0.25$ . The reason is that the POD captures the Karman vortex shedding, which is the most energetic structure in the flow dynamical behavior, while the resolvent analysis also captures the Karman vortex shedding according to  $St = 0.15$ . This result demonstrates the ability of the resolvent analysis to capture the flow dynamics at specific

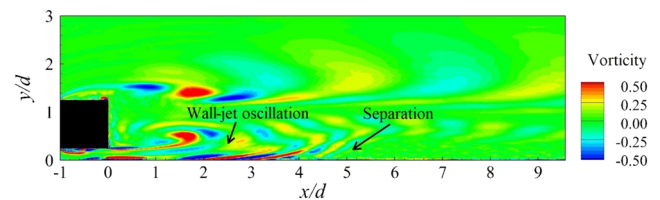
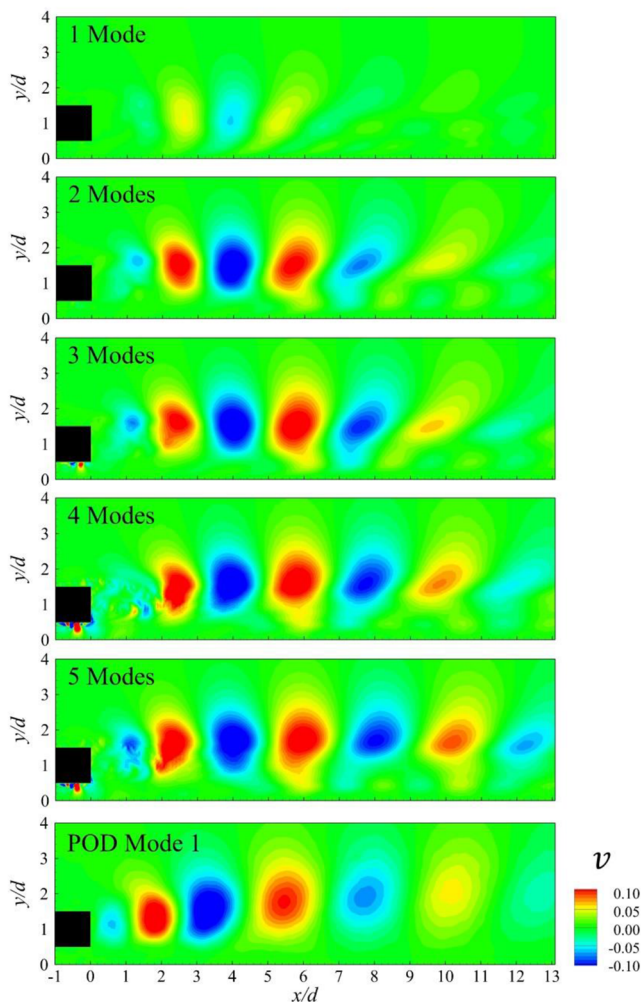


FIG. 15. Vorticity representation of the reconstructed field using the first five resolvent modes at  $St = 0.15$  and  $G/d = 0.25$ .



**FIG. 16.** Reconstructed fields using different numbers of resolvent mode at  $St = 0.15$  and  $G/d = 0.50$  and comparison with the POD mode.

frequencies. Furthermore, the reconstruction indicates that the resolvent modes that represent the wall jet oscillation make little contribution to the flow, demonstrating less intensified heat transfer immediately behind the rib than at  $G/d = 0.50$ .

## V. CONCLUSION

In this study, data assimilation was performed using the ABDA model with split fiber results as the observations to reproduce the mean fields of the flows behind a wall-proximity rib. Resolvent analysis was then applied on these mean flows to detect the optimal flow responses, which represent the energetic unsteady features, with respect to the turbulence forcing. The rib was located at gap ratios  $G/d = 0.25$  and  $0.50$ , and the flow Reynolds number was  $Re = 7600$  based on the rib size and free-stream velocity. The split fiber measurements were solely used as the observational data required in the data assimilation and resolvent analysis, while the TSP

and PIV results were used as the complement for analysis and validation.

Data assimilation using the streamwise velocity constraint at  $x/d = -0.25, 1.25, 4.25,$  and  $9.25$  of the observational data accurately reproduced the global mean fields in the cases of both gap ratios, including the wall jet originating from the gap, which was absent in PIV results due to spatial resolution limitations. The mean flow fields gave clear basis for the wall heat transfer properties and substantial heat transfer intensification immediately behind the rib. The global mean fields determined using the ABDA model were accurate and complete, including all boundaries and corner areas that were inaccessible in experiments, and were thus an excellent basis for the resolvent analysis.

The resolvent modes at Strouhal numbers  $St = 0.02, 0.05, 0.15,$  and  $0.30$  were subsequently obtained from the mean flows using a stochastic approach instead of performing the singular value decomposition (SVD) directly on the resolvent operator due to the large matrix size. With the help of the power spectral density of the split fiber measurement, the present resolvent analysis identified the large-scale flapping motion and the wall-jet fine scales, which enhanced the heat transfer in the case of  $G/d = 0.25$ , in addition to the Karman vortex shedding, which made little contribution to the wall heat transfer in the case of  $G/d = 0.50$ . The flow dynamical features in both cases were reconstructed using the leading five resolvent modes at  $St = 0.15$ , showing the convergence of the reconstruction with the increasing number of the resolvent modes and good agreement with the POD modes.

This study has proposed a new way of approaching unsteady flow by coupling stochastic resolvent analysis which avoids the calculations resulting from a large resolvent operator matrix, with the ABDA model which provides a computationally cheap method for mean flow determination. Its application is expected to be extended to general flow conditions without the limitations of monochromatic flow, parallel flow assumptions, and convective instability. Nevertheless, only two-dimensional perturbation is considered in the present resolvent analysis with spanwise wavenumber  $k = 0$ . The introduction of the spanwise wave will be definitely beneficial to the unsteadiness reconstruction; this gives an intention for the systematic investigation in future work.

## ACKNOWLEDGMENTS

The authors gratefully acknowledge financial support for this study from the National Natural Science Foundation of China (Grant No. 11725209).

## REFERENCES

- <sup>1</sup>J.-C. Han, S. Dutta, and S. Ekkad, *Gas Turbine Heat Transfer and Cooling Technology* (CRC Press, 2012).
- <sup>2</sup>F. P. Incropera, "Convection heat transfer in electronic equipment cooling," *J. Heat Transfer* **110**, 1097 (1988).
- <sup>3</sup>M. Meldi and A. Poux, "A reduced order model based on Kalman filtering for sequential data assimilation of turbulent flows," *J. Comput. Phys.* **347**, 207 (2017).

- <sup>4</sup>T. Suzuki, "POD-based reduced-order hybrid simulation using the data-driven transfer function with time-resolved PTV feedback," *Exp. Fluids* **55**, 1798 (2014).
- <sup>5</sup>R. Kikuchi, T. Misaka, and S. Obayashi, "Assessment of probability density function based on POD reduced-order model for ensemble-based data assimilation," *Fluid Dyn. Res.* **47**, 051403 (2015).
- <sup>6</sup>F. Gómez, H. M. Blackburn, M. Rudman, A. S. Sharma, and B. J. McKeon, "A reduced-order model of three-dimensional unsteady flow in a cavity based on the resolvent operator," *J. Fluid Mech.* **798**, R2 (2016).
- <sup>7</sup>M. Couplet, C. Basdevant, and P. Sagaut, "Calibrated reduced-order POD-Galerkin system for fluid flow modelling," *J. Comput. Phys.* **207**, 192 (2005).
- <sup>8</sup>V. L. Kalb and A. E. Deane, "An intrinsic stabilization scheme for proper orthogonal decomposition based low-dimensional models," *Phys. Fluids* **19**, 054106 (2007).
- <sup>9</sup>L. M. Hudy, A. Naguib, and W. M. Humphreys, "Stochastic estimation of a separated-flow field using wall-pressure-array measurements," *Phys. Fluids* **19**, 024103 (2007).
- <sup>10</sup>A. Garcia-Sagrado and T. Hynes, "Stochastic estimation of flow near the trailing edge of a NACA0012 airfoil," *Exp. Fluids* **51**, 1057 (2011).
- <sup>11</sup>X. Jin, P. Cheng, W.-L. Chen, and H. Li, "Prediction model of velocity field around circular cylinder over various Reynolds numbers by fusion convolutional neural networks based on pressure on the cylinder," *Phys. Fluids* **30**, 047105 (2018).
- <sup>12</sup>Z. Wang, K. Luo, D. Li, J. Tan, and J. Fan, "Investigations of data-driven closure for subgrid-scale stress in large-eddy simulation," *Phys. Fluids* **30**, 125101 (2018).
- <sup>13</sup>B. Pier, "On the frequency selection of finite-amplitude vortex shedding in the cylinder wake," *J. Fluid Mech.* **458**, 407 (2002).
- <sup>14</sup>S. Mittal, "Global linear stability analysis of time-averaged flows," *Int. J. Numer. Methods Fluids* **58**, 111 (2010).
- <sup>15</sup>D. Barkley, "Linear analysis of the cylinder wake mean flow," *Europhys. Lett.* **75**, 750 (2006).
- <sup>16</sup>D. Sipp and A. Lebedev, "Global stability of base and mean flows: A general approach and its applications to cylinder and open cavity flows," *J. Fluid Mech.* **593**, 333 (2007).
- <sup>17</sup>T. K. Sengupta, N. Sharma, and A. Sengupta, "Non-linear instability analysis of the two-dimensional Navier-Stokes equation: The Taylor-Green vortex problem," *Phys. Fluids* **30**, 054105 (2018).
- <sup>18</sup>P. Caillol, "A singular vortex Rossby wave packet within a rapidly rotating vortex," *Phys. Fluids* **29**, 046601 (2017).
- <sup>19</sup>D. Dasgupta, S. Nath, and D. Bhanja, "Dual-mode nonlinear instability analysis of a confined planar liquid sheet sandwiched between two gas streams of unequal velocities and prediction of droplet size and velocity distribution using maximum entropy formulation," *Phys. Fluids* **30**, 044104 (2018).
- <sup>20</sup>B. J. McKeon and A. S. Sharma, "A critical-layer framework for turbulent pipe flow," *J. Fluid Mech.* **658**, 336 (2010).
- <sup>21</sup>S. Beneddine, D. Sipp, A. Arnault, J. Dandois, and L. Lesshafft, "Conditions for validity of mean flow stability analysis," *J. Fluid Mech.* **798**, 485 (2017).
- <sup>22</sup>S. Beneddine, R. Yegavian, D. Sipp, and B. Leclaire, "Unsteady flow dynamics reconstruction from mean flow and point sensors: An experimental study," *J. Fluid Mech.* **824**, 174 (2017).
- <sup>23</sup>C. He, Y. Liu, and L. Gan, "A data assimilation model for turbulent flows using continuous adjoint formulation," *Phys. Fluids* **30**, 105108 (2018).
- <sup>24</sup>C. He, Y. Liu, D. Peng, and S. Yavuzkurt, "Measurement of flow structures and heat transfer behind a wall-proximity square rib using TSP, PIV and split-fiber film," *Exp. Fluids* **57**, 165 (2016).
- <sup>25</sup>O. Semeraro, V. Jaunet, P. Jordan, A. V. Cavalieri, and L. Lesshafft, *Stochastic and Harmonic Optimal Forcing in Subsonic Jets* (Lyon, France, 2015).
- <sup>26</sup>A. P. Singh, S. Medida, and K. Duraisamy, "Machine-learning-augmented predictive modeling of turbulent separated flows over airfoils," *AIAA J.* **55**, 2215 (2017).
- <sup>27</sup>P. Spalart and S. Allmaras, "A one-equation turbulence model for aerodynamic flows," *Recherche Aérospatiale* **1**, 5 (1994).
- <sup>28</sup>C. Othmer, "A continuous adjoint formulation for the computation of topological and surface sensitivities of ducted flows," *Int. J. Numer. Methods Fluids* **58**, 861 (2008).
- <sup>29</sup>L. Armijo, "Minimization of functions having Lipschitz continuous first partial derivatives," *Pac. J. Math.* **16**, 1 (1966).
- <sup>30</sup>G. Dergham, D. Sipp, and J.-C. Robinet, "Stochastic dynamics and model reduction of amplifier flows: The backward facing step flow," *J. Fluid Mech.* **719**, 406 (2013).
- <sup>31</sup>J. L. Lumley, *Stochastic Tools in Turbulence* (Academic Press, New York, London, 2012).
- <sup>32</sup>L. Sirovich, "Turbulence and the dynamics of coherent structures. I. Coherent structures," *Q. Appl. Math.* **45**, 561 (1987).